Status review of air breathing electric propulsion experimental research at UC3M

IEPC-2024-773

Andrés Rabuñal-Gayo [*] , Pablo Fajardo[†] , Marco R. Inchingolo[‡] and Jaume Navarro-Cavallé[§]
Department of Aerospace Engineering, Universidad Carlos III de Madrid, Leganés, Spain.

This manuscript presents the results of the first test performed in our laboratory targeting the use of a Helicon Plasma Thruster for the Air-breathing electric propulsion concept. ABEP will presumably be a central key technology for enabling sustainable missions at very low Earth orbit missions. This preliminary study inquires on the assessment of propulsive performances, operating the thruster at different air flow rates, 4.5-27 sccm Air, keeping constant the radiofrequency power, 400 W, and magnetic field strength at the magnetic throat, 600 G. The thruster characterization relies only on a reduced set of electrostatic probes, concluding that power conversion efficiency is about 4%. No signs of degradation have been detected neither at thruster nor at facility level due to the use of atmospheric air as propellant.

I.   Introduction

Electric propulsion is a well-established technology for in-space applications. The interest in exploiting very low Earth Orbits (VLEO) has raised in the last years, aiming to improve the performance of some missions such as Earth Observation. Reducing the altitude of the orbit is beneficial[1] in terms of a lower launch cost, improved spatial and temporal resolution, increased performance in communications and link budget, lower radiation environment, easier disposal of the satellite at the end of the mission, and the implementation of aerodynamic payloads or control.

The possibility of breathing the gases present at those high-altitude layers of the Earth's atmosphere (ABEP concept[2]) and use it as propellant is a critical development to allow the operation of a satellite in VLEO. Although different propulsion systems have been studied in the literature[3] , most of the efforts have been focused on well-established technologies like Hall Thrusters, both from an experimental perspective[4] , theoretical and simulation studies[5] and feasibility and mission concept works[6] .

On the other side, electrodeless plasma thrusters (EPT), apart from being presented as an alternative to traditional electric propulsion systems, have also been suggested for ABEP. The main candidate within this field is the RF/Helicon-based thruster (HPT)[7,8,9] . An HPT is a technology that comprises for the general case a cylindrical discharge chamber made of dielectric walls, a gas inlet typically situated at the rear of the chamber, an external inductor/antenna emitting the RF power to be absorbed by the plasma, and an external solenoid generating a magnetic field (Magnetic Nozzle[10]), typically in the range between 100 and 1000 G.

At the current state of the art, there are 2 main areas related to the thruster technology that limit the feasibility of ABEP[11] : (1) Air-compatible cathode technology; (2) Techniques to improve propellant utilization on atmospheric species. On one hand, EPTs eliminate the need for electrodes, so the challenges related to cathodes and neutralizers for ABEP do not apply to this technology, while this is a critical aspect

---

in the development of an ABEP-oriented HT. On the other hand, although propellant utilization is typically low in EPTs, there is evidence in the literature (see Ref. 12) that suggests that HT operating at low voltages suffer from poor propellant utilization efficiency, especially when using alternative propellants, but using an RF-augmented system may increase the propellant utilization efficiency. Another important advantage of EPT in comparison with HT is that these devices are typically operated at lower power, reducing the need for increased solar panel area and, therefore, reducing the drag of the satellite and the thrust needed to maintain the orbit.

In this work, we present the preliminary results obtained using the HPT breadboard platform[13,14,15] when fed with atmospheric air. The test campaign consists of a parametric analysis of the influence of the variation of the mass flow rate while the rest of the HPT parameters remain constant. The performance of the HPT and the plasma plume properties are probed using electrostatic diagnostics.

The paper is organized as follows. In section II, the HPT, the test facility and the electrostatic probes are presented. Secondly, in section III the methodologies applied for the probe data post-processing are derived. In section IV the results of an HPT air-breathing experimental campaign are shown and compared, in terms of plume properties and thruster performance, with respect to a recent Krypton-fed test campaign. Lastly, in section V the conclusions extracted from this work are drawn.

II. Experimental setup

The HPT prototype employed in this test campaign is the thruster unit breadboard model developed jointly by Sener Aeroespacial and Universidad Carlos III de Madrid[14]. The device is a compact low-power-class HPT with a 25 mm inner diameter and a 140 mm source length, made of quartz. The propellant is injected through an injector plate located at the rear of the discharge tube, made of Macor®. The RF power, 400 W at 13.56 MHz, is generated by the RF Seren 2001 amplifier. RF power is coupled to the antenna via a customized π-type matching network to maintain system impedance matched across all operational conditions. Reflected power is kept below 2%, for all the tests. A convergent-divergent external magnetic field is generated by a single solenoid. Its peak (throat of the magnetic field, located 2 cm upstream of the quartz outlet), has a strength of 600 G for the reference case. The main components of the HPT are drafted in Fig. 1.
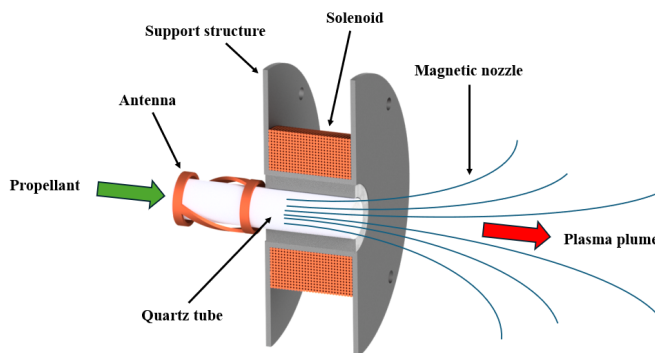

Figure 1. Main components of the HPT prototype.

The vacuum chamber[16] consists of a stainless-steel 304 cylinder 3.5 m long, with an inner diameter of 1.5 m. The chamber is equipped with the following vacuum technologies: a dry mechanical pump Leyvac LV80, two magnetically levitated turbo-molecular pumps Leybold MAGW2.200iP, and three cryopanels Leyvac 140 T-V. Pressure is monitored by using combined Pirani and Bayard-Alpert gauges in the Ionvac-Leybold sensor, with full range $5 \cdot 10^{-10}$- 1000 mbar. Ultimate pressure in dry conditions is about 10^{-7} mbar. During the Krypton-fed tests, the flow rate was controlled by a Bronkhorst EL-FLOW Select Xenon calibrated mass flow controller, with a resolution of 0.1 sccm and 100 sccm full range. For the air-fed tests, air flow was controlled by a multiple gas calibrated Alicat MC-100SCCM-D mass flow controller. The performance of Alicat/Bronkhost devices were compared against each other to reproduce the same flow to vacuum pressure curve. Then, a correction factor can be applied to operate under identical flow conditions, independently of the controller and gas used.

Electrostatic probes can be moved along the plasma plume by using a robotic arm system. This system displaces the probe holder in a polar reference frame (R - θ), which lays on the horizontal plane that virtually cuts the thruster in two halves. The center of this polar frame is aligned with the HPT outlet section (see Fig. 2). The radial range is 0-400mm, while the azimuth one is -90 to 90 deg.. The resolution of the system is about 1 mm and 1 deg, with uncertainties $\pm$ 0.3 mm and $\pm$ 0.3 deg, for the radial and the azimuth directions, respectively.
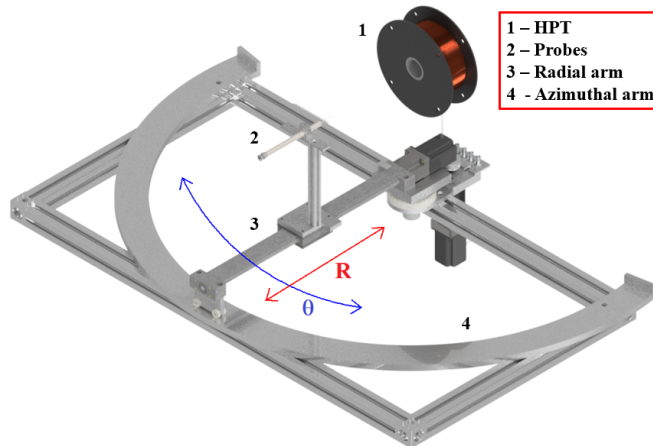

Figure 2. CAD render of the experimental setup. (1) is the thruster solenoid, (2) is the probe holder, (3) is the radial carriage, and (4) is the rail that allows for the azimuthal rotation.

In this work, the set of diagnostics relies only on electrostatic probes. Among them, an RF-compensated Langmuir probe (LP hereafter), with a cylindrical main electrode, 6 mm long and 0.254 mm in diameter. The secondary electrode for RF compensation has a surface ∼83 times larger than the main tip. RF chokes are tuned at 13.56 and 27.12 MHz. This will resolve the plasma (ion) density, plasma potential and electron temperature. The LP tip is biased with respect to the vacuum chamber ground using a Keithley 6517B electrometer.

A Faraday cup (FC), developed in-house as well as the LP, will determine the ion current density[17], the same electrometer is used to measure the collected current. The aperture of the cup is 10 mm, and it is typically biased at -150 V with respect to chamber ground. This value has been determined based on the FC I-V curve at different operating conditions of the thruster. The bias at -150 V ensures the FC is working in the ion saturation regime. Lastly, a retarding potential analyzer (RPA), Semion Unit by Impedans, is used to resolve the ion velocity distribution function[18]. The model employed in this work implements a collector electrode and a total of 4 independently biased grids: an orifice grid, an electron repelling grid, a retarding potential grid to filter the different ions according to their axial energy, and a secondary electron suppression grid, which is used to reduce the spurious signal due to secondary electrons emitted from the collector plate due to ion impacts. For all the scans completed in this work, the orifice grid was kept at floating potential. The plasma electron repeller grid and the secondary electron repeller grid were biased at -60 and -70 V, respectively. The electrode collector was biased at -60 V. The retarding potential grid was swept from 0 V to 250 V in steps of 1 V.

III. Methodology

This section summarizes the different methodologies implemented to retrieve useful data from the diagnostics introduced in Section II, with the final goal of assessing HPT air-fed performances. Due to the chemical peculiarities of ionizing atmospheric air, the plasma-probes model becomes cumbersome. For most of them, the plasma properties characterization is not complete enough (e.g. degree of dissociation) to tune the models accordingly. In such a case, the decision taken goes in the direction of underlining, whenever possible, the variability of the results depending on the considered hypotheses.

A. Ion beam current and discussion of the plume molecular composition

The ion current density at any point, $j_i(R, \theta)$, is computed by dividing the collected current I_{FC} by the aperture area of the FC , $A_{FC} = 78.5 \ mm^2$, $j_i = I_{FC}/A_{FC}$. The ion current density profile is measured along arcs of constant radius, R = 300 mm and R = 400 mm from the exhaust of the HPT, from -90 to 90 deg, with an angular resolution of 2 deg for $|\theta| >= 20$ deg and 1 deg for $|\theta| < 20$ deg. For each scenario, 2 azimuth sweeps are performed and post-processed independently. As briefly commented above, before proceeding with the $j(\theta)$ scan, the FC I-V curve is measured to determine the bias to ensure the FC operates within the ion saturation regime.

Once $j(\theta)$ is known, this is integrated over the hemispherical surface of radius R, in order to compute the total ion beam current[17] , I_b:

$$I_b = \pi R^2 \int_{-\pi/2}^{\pi/2} j_i(\theta) \, |\sin(\theta)| \, d\theta. \tag{1}$$

This assumes, among other assumptions, that all ions are singly charged. It considers as well the axial symmetry of the current density profile, being this $j(\theta) = 0.5(j(\theta) + j(-\theta))$. It is assumed that the FC measures the current density in the direction perpendicular to its front face (aperture). Considering the arm system, this means that the FC direction of acquisition is always radial with respect to the HPT outlet section. However, the flow is not necessarily aligned with the probe, except for the ideal case of a conical beam expansion.

The propellant utilization efficiency, η_u, can be estimated based on the previous ion beam current and the propellant mass flow rate,

$$\eta_u = \frac{I_b m_i}{\dot{m}}. \tag{2}$$

in which m_i is the average mass of ions. For the sake of simplicity, only singly charged ions are considered. Concerning m_i more details will be given since this depends on the composition of the ion beam from a molecular point of view.

Analogously, the axial ion beam current, I_z can be computed by integrating the cosine weighted ion current density over the hemisphere, thus considering the axial projection of the local current density. The same hypotheses as in Eq. (1) apply as well.

$$I_z = \pi R^2 \int_{-\pi/2}^{\pi/2} j_i(\theta) \cos(\theta) \, |\sin(\theta)| \, d\theta. \tag{3}$$

Based on these axial and total ion beam current, the beam divergence efficiency can be estimated as,

$$\eta_{div} = \left(\frac{I_z}{I_b}\right)^2. \tag{4}$$

If the plume composition varies substantially with θ, then both I_z and I_b should be carefully computed considering a different ion average mass m_i at each θ angle. In this work, constant m_i with θ is taken for simplicity. Nevertheless, a proper value for m_i is still necessary in Eq. (2). This value is largely impacted by the molecular composition of the mixture, more precisely, by the degree of oxygen and nitrogen dissociation, β_{O_2}, β_{N_2} respectively. These betas range from 0 to 1, for null and complete dissociation respectively. If these betas were measured, then $m_i = \sum_j \chi_j m_j$, with χ_j the molar fraction of each species of mass m_j. Note the latest just depend on betas, $\chi_j = \chi_j(\beta_{O_2}, \beta_{N_2})$.

$$m_i = \sum_j \chi_j(\beta_{O_2}, \beta_{N_2}) m_j \tag{5}$$

β values might be adjusted based on the analysis of the dissociation and ionization rates. These rates depend on the the electron temperature, energy cost of each process and the cross section of each process. First, the energy cost of dissociation and ionization is presented in Table 1, indicating the reference from where these have been taken. The energy required for O_2 dissociation is about half of the energy required to dissociate N_2. Both energy thresholds are below the rest of the ionization processes of atomic or diatomic molecules, that go from 12 eV up to 15.6 eV, with this order, $E_{ion,O_2} < E_{ion,O} < E_{ion,N} < E_{ion,N_2}$. Then it

Process	E_j (eV)	E_j Ref.	$\sigma_j(Te)$ Ref.
N_2 dissociation	9.76	[19]	[20]
N_2 ionization	15.58	[21]	[21]
N ionization	14.54	[21]	[21]
O_2 dissociation	5.16	[22]	[23]
O_2 ionization	12.07	[21]	[21]
O ionization	13.6	[21]	[21]

Table 1. Energy thresholds, E_j, for different dissociation/ionization processes, and its reference. The reference used to model each cross section σ_j is also included in the last column.

is expected that oxygen dissociation will dominate against nitrogen dissociation, meaning that $\beta_{O_2} \neq \beta_{N_2}$, which opposes the previous reasoning.

Each collision rate R_j can be evaluated by assuming Maxwellian electrons at T_e, and a well-characterized cross-section $\sigma_j(T_e)$ together with the mentioned energy thresholds.

$$R_j\left(T_e\right) = \sqrt{\frac{8k_B T_e}{\pi m_e}} \frac{\sigma_j\left(T_e\right)}{e^{\frac{E_j}{T_e}}} \left(1 + \frac{\frac{E_j}{T_e}}{\left(1 + \frac{E_j}{T_e}\right)^2}\right). \tag{6}$$

Index j refers to each collisional process. Figure 3 shows $R_j(T_e)$. Dissociation of molecules and ionization of atomic species are more common than diatomic molecules ionization processes.
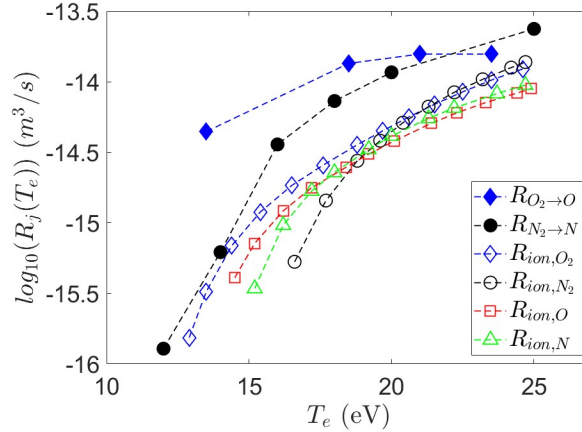

Figure 3. Collision rates for the different events $R_j(T_e)$.

The production rate of generated new species, j_2, from species j_1 is $\dot{n}_{j2} = n_e n_{j_1} R_{j2}$. Unfortunately, no information was gathered about the plume's chemical composition, thus, only assumptions can be made. The injected atmospheric air (not accounting for the fraction of water dissolved in it, air humidity, and other minor traces) can be assumed ideally, so there are 3.76 N_2 particles per particle of O_2. Nevertheless, $R_{O_2 \to O} \gg R_{N_2 \to N}$ below 15 eV, meaning that $\beta_{O_2} \geq \beta_{N_2}$. But, for the sake of simplicity, in Eq. (2) we take $\beta_{O_2} = \beta_{N_2} = \beta$ in order to simplify the value for the average mass $m_i = 28.84/(1 + \beta)$ Da $= 4.78 \cdot 10^{-26}/(1 + \beta)$ kg. Then, full dissociation (and equal for oxygen and nitrogen) is modeled taking $\beta = 1$, while null dissociation ($\beta = 0$) is very unlikely in our case. Note also that $\beta = 1$ is the most conservative limit for η_u estimation. An important remark is still necessary, despite the uncertainties on β_{O_2}, β_{N_2} the error in the estimation of m_i is not strongly impacted by the difference between betas thanks to the fact that oxygen and nitrogen atomic masses are similar (the difference is only 14 %). Obviously, it is strongly sensible to the value of β itself, because of the factor 2 between the diatomic/atomic masses, thus this represents an uncertainty of 50 % in the estimation of m_i and consequently on η_u.

B. Spatially resolved plasma properties and ion energy distribution function

The analysis of the LP I-V characteristic curve can be used to determine the 2D map of local plasma properties, such as density (ion density n), plasma potential V_p and electron temperature T_e. The post-processing is performed relying on the orbital motion limited (OML) theory[24, 25], which gave, in general, the best matching results although in a small number of cases, the sheath regime may be closer to transitional. Taking the assumption of quasineutrality, n_i is obtained from the linear fit of the collected current I in the ion saturated regime, $V_b \ll V_f$ (V_f is the floating voltage). T_e is computed as the inverse of the $\log(I_e) - V$ slope. Finally, V_p is determined by the inflection point method, finding the voltage that corresponds to the peak of the first derivative of the I-V curve, $\max(dI/dV)$.

For the $\dot{m} = 9.32$ sccm Air and $\dot{m} = 27$ sccm Air scenarios, plasma plume properties were scanned between R = 100 mm and R = 300 mm, in steps of 25 mm, and θ = -30 deg to θ = 50 deg, in steps of 5 or 10 deg. For the $\dot{m} = 18$ sccm Air case, only on-axis measurements were taken ($\theta = 0$ deg, $R \in 100 - 300$ mm). At least two I-V curves are measured at each location and these are post-processed separately, without averaging them together.

The ion energy distribution function (IEDF) can be determined by differentiating the I-V curve provided by the RPA[26]. The resulting I-V curve is affected by noise, especially far from the center line of the plume where the ion current drops. To avoid noise-induced errors in the post-processing, the I-V curve is smoothed by applying a moving average of size 2. At each location, 3 I-V curves, were scanned and they were post-processed independently. Once the IEDF (or f_{E_i}) is resolved, it is possible to determine the most probable energy of the ions, $E_i = max(f_{E_i})$, and the average ion energy $\widehat{E}_i$. The most different result among the three independent I-V traces was discarded and the final value of $E_i \, max(f_{E_i})$ and $\widehat{E}_i$ were computed as the average of the 2 remaining.

$$\widehat{E}_i = \frac{\int_{E_{i,min}}^{E_{i,max}} E_i f_{E_i} \, dE_i}{\int_{E_{i,min}}^{E_{i,max}} f_{E_i} \, dE_i},$$ (7)

with $E_{i,min} = 0$ and $E_{i,max} = 250$ eV.

The thruster energy conversion efficiency, η_{conv}, is estimated as

$$\eta_{conv} = \frac{P_b}{P},$$ (8)

in which P is the RF power delivered to the HPT, and P_b is the beam power. For the latest, we are going to consider only the power coming from the ion energy, while discarding the residual energy on electrons. It is possible to roughly estimate P_b by combining $j_i(\theta)$ and $\widehat{E}_i(\theta)$, defining the ion energy density as $j_i\widehat{E}_i$. Since the ion energy is referred to ground, this energy density is not only the ion kinetic energy, it includes the potential energy too. Note that $j_i\widehat{E}_i$ can only be determined in the locations where the IEDF has been measured. Then a set of Gaussian curves are used to fit $j_i\widehat{E}_i$, obtaining the fitted curve $(j_i\widehat{E}_i)^\star$, which is used to determine P_b. The fitted curve is depicted as an example in Figure 4.

$$P_b = \pi R^2 \int_{-\pi/2}^{\pi/2} (j_i\widehat{E}_i)^\star |\sin(\theta)| \, d\theta.$$ (9)

Another approach for P_b can be obtained directly from the ion beam current and the azimuth averaged ion mean energy,

$$P_b \approx I_b < \widehat{E} >,$$ (10)

which in fact yields similar results. The discrepancy against Eq. (9) is small thanks to the fact that the ion mean energy shows a small variation along the azimuth direction, as it will be presented next.

IV.   Results

For all the cases analyzed in this section, the RF power (400 W forward, with less than 2% of reflected power) and the magnetic field (600 G at the throat) are kept constant throughout the entire experiment.
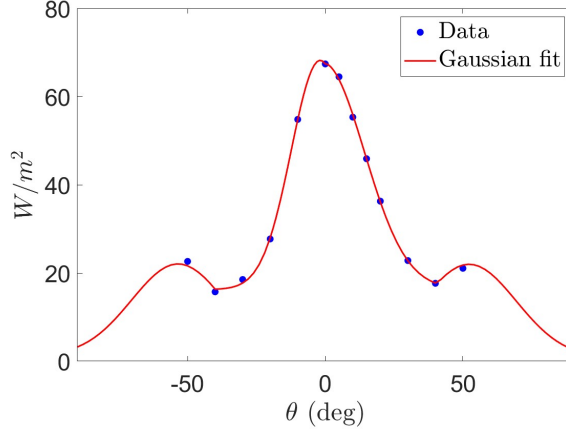
Figure 4. Optimized gaussian fit of the ion kinetic energy ($\dot{m} = 27$ sccm Air, R = 400 mm).

In a previous campaign, the same thruster unit had been characterized for Krypton as propellant, with a flow rate of $\dot{m} = 9.32$ sccm Kr. This case is taken as a reference for the comparison of air versus noble gas operation of the HPT. Fair and natural comparisons can be made in terms of (1) same volumetric flow rate, $\dot{m} = 9.32$ sccm Air; (2) same mass flow rate, which requires to increase the flow to $\dot{m} = 27$ sccm Air; and (3) some intermediate/near points, i.e. 4.5, 13.5, 18 and 22.5 sccm Air.

Visual inspection of the HPT operating with air is shown in Figure 5. The characteristic orangish/pinkish color is observed in the plume and source. The brightness increases with the flow rate, but seems to saturate beyond 18 sccm Air.

| 4.5 sccm Air | 9.32 sccm Air | 13.5 sccm Air | 18 sccm Air | 22.5 sccm Air | 27 sccm Air |

Figure 5. Plasma plume of the HPT operating with air under different conditions (from left to right: 4.5, 9.32, 13.5, 18, 22.5 and 27 sccm Air).

Another drawback of air operation is that the cryopanels are not designed to trap gases as light as those produced in this experiment. This penalizes the vacuum chamber's performance. The average trend of $P_{ch}(\dot{m})$ is depicted in Figure 6. The effect of background pressure on the LP measurements has been analyzed for some plume locations (R = 100 mm and R = 300 mm, for $\theta = 0$ deg to $\theta = 50$ deg in steps or 5 or 10 deg. A total of 16 points were used for the statistic analysis). Table 2 provides an example of density, plasma potential and electron temperature variation due to operating the HPT at different pressure levels, ranging from $6.5 \cdot 10^{-6}$ mbar to $3.2 \cdot 10^{-5}$ mbar.

	P_1/P_2	n_{i_1}/n_{i_2}	V_{p_1}/V_{p_2}	T_{e_1}/T_{e_2}
Max. difference (%)	+386	+32	+31	-15

Table 2. Variability of the LP results due to differences in the background pressure. P_{ch} between $6.5 \cdot 10^{-6}$ mbar and $3.2 \cdot 10^{-5}$ mbar, $\dot{m} = 27$ sccm Air, properties measured at R = 100 and R = 300 mm, from $\theta = 0$ deg to $\theta = 50$ deg.
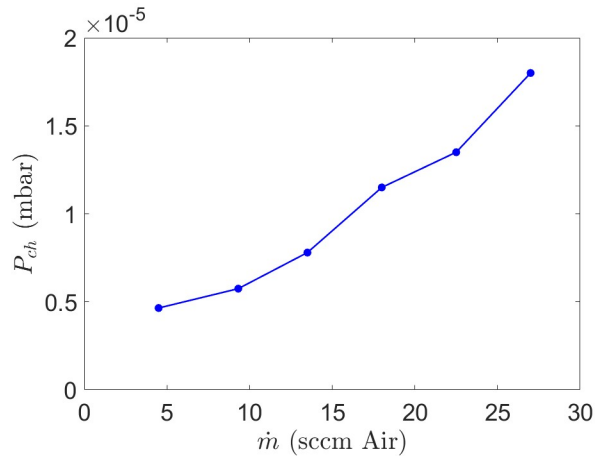
Figure 6. Evolution of $P_{ch}(\dot{m})$ during the experimental campaign for the ion beam current data.

A.   Ion beam current, propellant utilization and plume divergence

The ion current density profiles $j_i(\theta)$, measured at $R = 300, 400$ mm, are shown in Figure 7. Krypton results at 9.32 sccm Kr are depicted together as a reference, pointing out that all cases with air present a higher current density (at least at the plume center, on the axis). This could be considered as an unexpected result, but it is not, in fact, it is a confirmation that oxygen/nitrogen dissociation probably dominates the RF-air plasma discharge as discussed in Section III-A. Dissociation increases, might potentially double, the number of single atoms available for ionization, thus leading to larger current densities, for the same particle flow rate of neutral gas.

Increasing $\dot{m}$ yields the increase of its side lobes, which have been identified as well in previous works[27]. While the center peak increases up to the case at 13.5 sccm Air, at higher flow rates the central peak decreases. These profiles translate into the saturation of the ion beam current, I_b, for $\dot{m} \geq 13.5$ sccm Air, which is illustrated in the same figure group. Concerning the axial current, I_z, the fact that more current is allocated at the sides lobes when the neutral flow is increased makes I_z present a maximum (approximately at 18 sccm Air) and beyond it, axial current starts to decrease.

The final consequence of the ion current density is that both η_u and η_{div} monotonically decrease with $\dot{m}$. The appearance of the side lobes extracts current from the center of the beam and takes it to the outer regions, causing a decrease in divergence efficiency. Concerning η_u, depicted results are computed assuming $\beta = 1$, full dissociation. Below 13.5 sccm Air, the increase rate of I_b is lower than the flow rate increase, so there is no gain in terms of propellant utilization, while the penalization is higher beyond 13.5 sccm Air due to the the saturation of I_b.

Table 3 presents the impact of m_i, or equivalently the values of β_{O_2}, β_{N_2}, on the estimation of η_u. The comparison between $\beta_{O_2} = \beta_{N_2} = \beta = 1$ against $\beta_{O_2} = \beta_{N_2} = \beta = 0$, i.e. full versus null dissociation, is trivial, for null dissociation η_u is doubled. These two cases set the lower/upper limits, and the rest of the combinations lay within this range.

Scenario	m_i (Da)	η_u (%)
Full dissociation, $\beta_{O_2} = \beta_{N_2} = 1$	14.42	3.86-8.91
Null dissociation, $\beta_{O_2} = \beta_{N_2} = 0$	28.84	7.73-17.82
$\beta_{O_2} = 1, \beta_{N_2} = 0$	23.83	6.39-14.73
$\beta_{O_2} = 0, \beta_{N_2} = 1$	16.11	4.32-9.96
$\beta_{O_2} = \beta_{N_2} = 0.5$	19.22	5.15-11.88

Table 3. η_u under different plume compositions defined by the dissociation factors β_{O_2}, β_{N_2}.

The Krypton reference case lays below in terms of I_z and η_{div}, while it lays above in I_b and η_u.
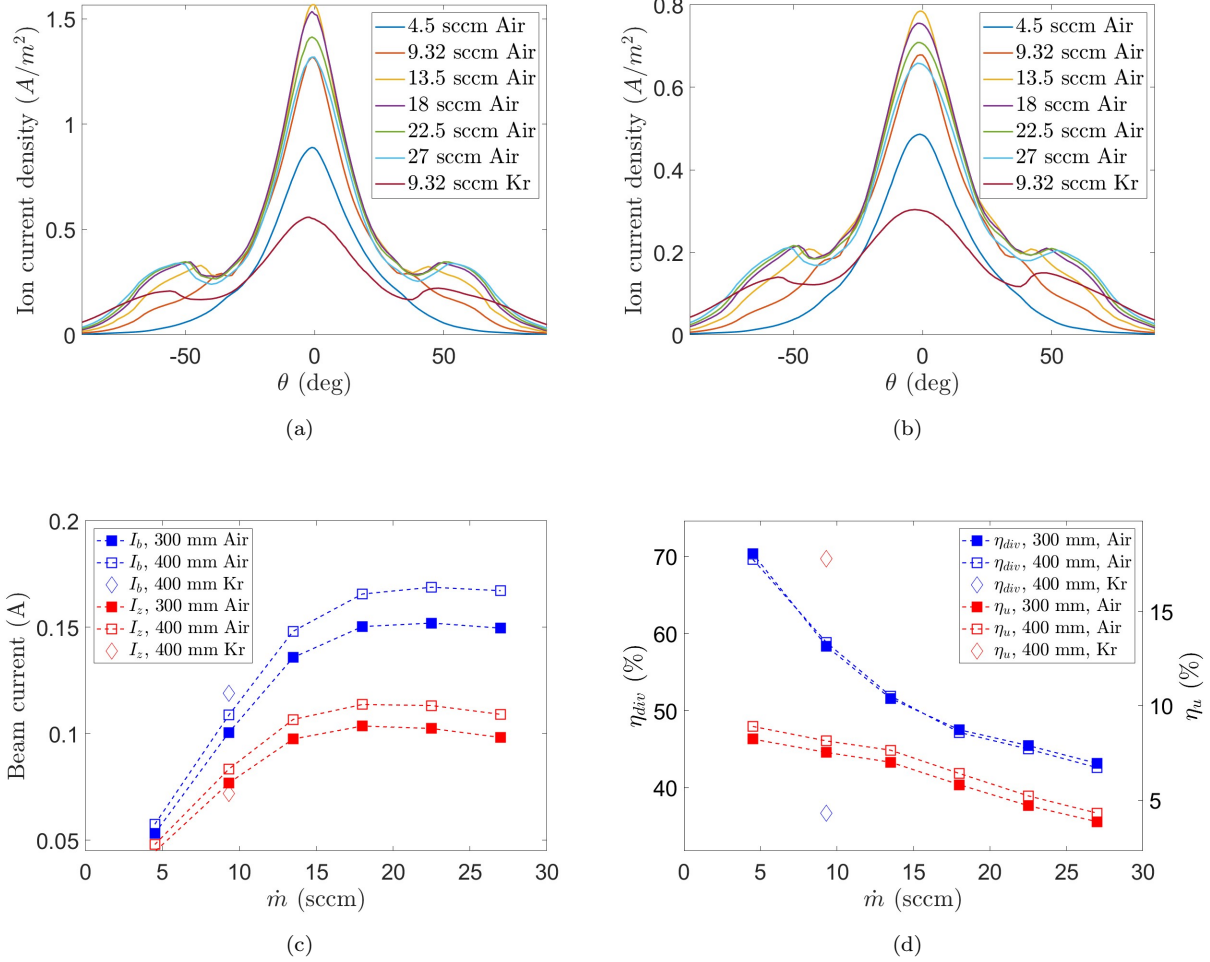
Figure 7. Ion current density profiles for R = 300 mm (top left) and R = 400 mm (top right), total ion current I_b and axial ion current I_z (bottom left) and propellant utilization η_u and divergence efficiency η_{div} (bottom right).

B. 2D plasma properties

Figure 8 shows the spatially resolved plasma properties. For the $\dot{m} = 9.32$ sccm Air (left column) and $\dot{m} = 27$ sccm Air (right column), measurement positions are represented with black dots and the maps were generated using a 2D linear interpolation of the experimental data. All the parameters show a slight asymmetry with respect to the center-line of the HPT, with higher values in the negative θ region, and decrease smoothly with distance. Ion density is concentrated in the main beam, decaying along the axial and azimuthal directions. Density increases with with $\dot{m}$. Electron temperature is maximized at the plume edges, showing two clear peaks around $\theta = \pm 30$ deg (9.32 sccm Air case). The increase in mass flow rate makes the temperature cool faster, and the regions of high temperature are localized close to the thruster. As usual in EPTs low mass flow rate regime is linked to higher T_e and more efficient propellant utilization. This non-uniformity of the temperature is expected to impact on the mixture composition, i.e. different degrees of dissociation and consequently different ionization fractions for each ion species depending on θ.

The plasma potential shows the common trend of quasi-neutral current-free plasmas expanding along a magnetic nozzle. These results prove that an important fraction of the ion acceleration occurs along the region explored and beyond. There is still residual electron energy at the downstream boundary, suggesting that the plume is still accelerating at that position. This is indicated by the temperature and potential levels measured there.
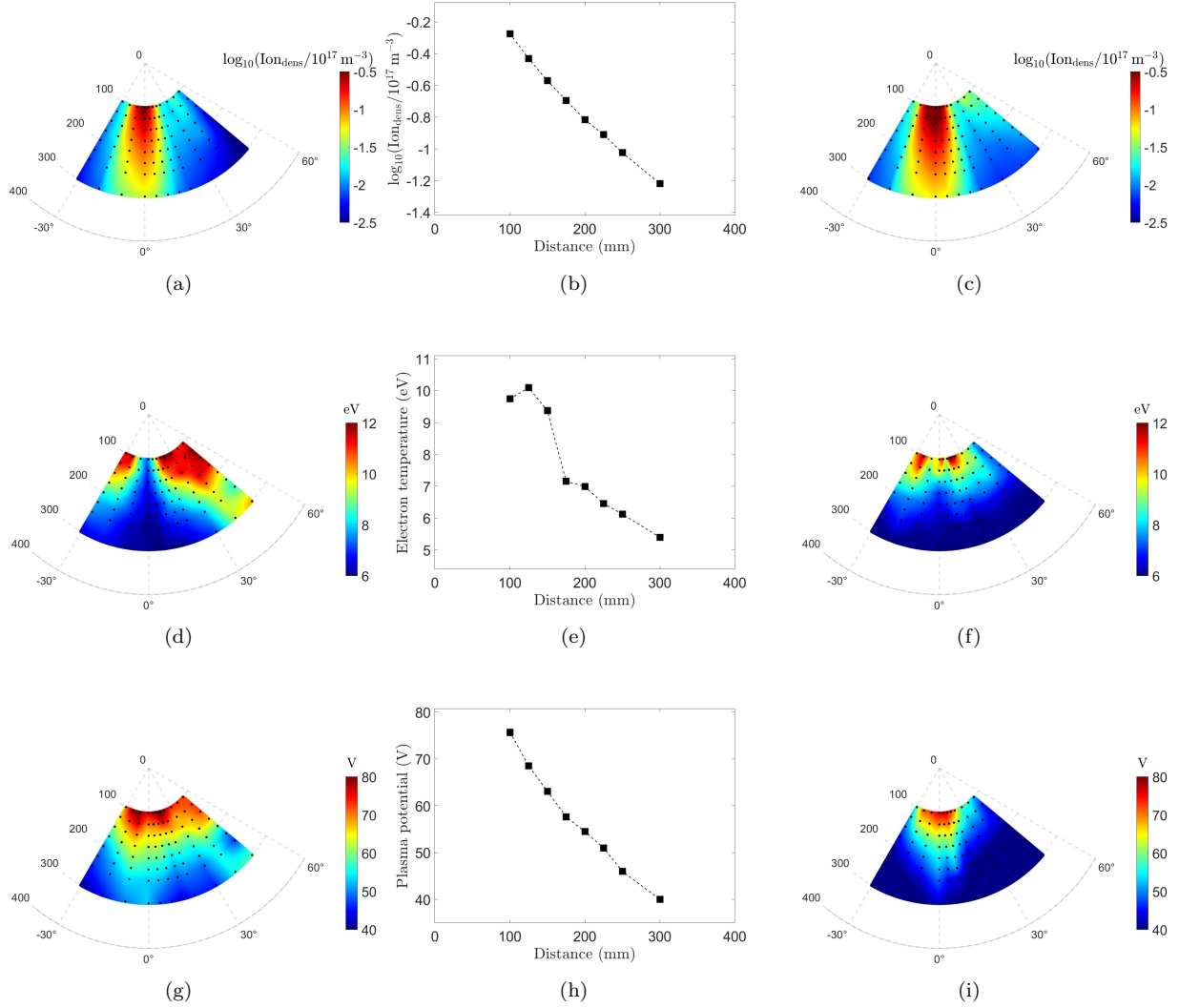
Figure 8. Ion densities (top row), electron temperatures (middle row) and plasma potentials (bottom row) for $\dot{m} = 9.32$ sccm Air (left column), $\dot{m} = 18$ sccm Air (middle column) and $\dot{m} = 27$ sccm Air (right column).

C.   Ion energy and thruster propulsive efficiency

Figure 9 shows the results obtained from the analysis of the IEDF. For all presented cases, a small asymmetry with respect to the center-line of the HPT can be appreciated. Overall, average ion energy increases with the propellant flow rate. Ion mean energy seems to increase at the edge of the plasma beam, see as reference $\theta = \pm 40, 50$ deg. This can be justified by the higher T_e measured at those angles. Despite the composition, in electrodeless plasma thrusters, higher electron temperature leads to larger ion energies[28] . This high temperature can also introduce changes in the plume composition, and consequently in the IEDF and its average.

Looking accurately at the different IEDF, at high flow rates (27 sccm Air), Figure 9 (e-f), the measurement taken on-axis shows the formation of a presumably secondary ion population at lower energies. The origin of this ion energy spread can be attributed to different mechanisms: changes in the composition or spread of the ionization region. In other previous works as in Ref. 18 , CEX collisions induced the formation of a low ion energy population, but it was found at much lower energies. In the cases presented here, the widening of the IEDF could be induced by the reasonably similar masses of the different species involved, e.g. it is not possible to distinguish between O or N ions.

Finally, as explained in Section III-B it is possible to compute the energy conversion efficiency, which is a
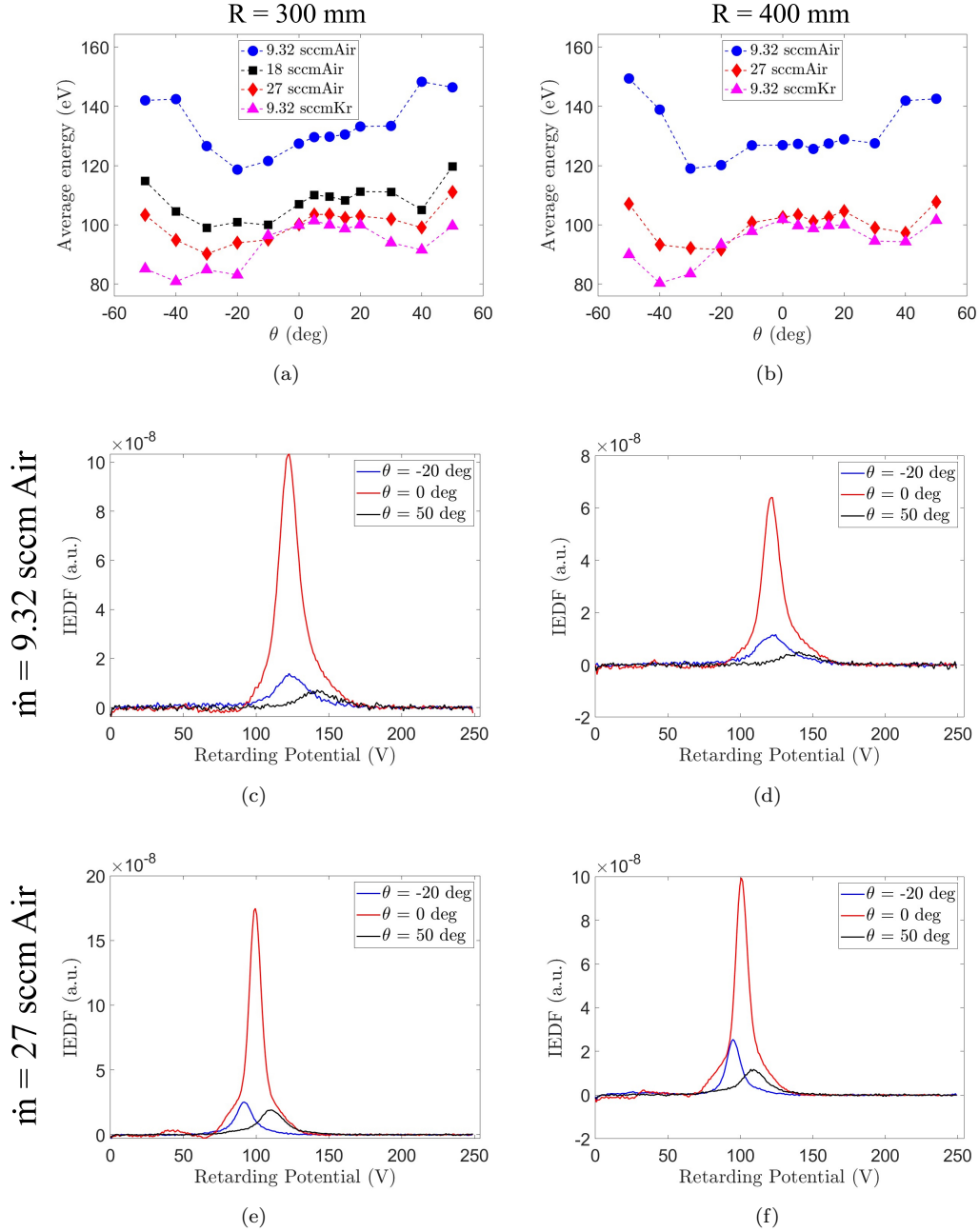
Figure 9. Ion Average energy (top row) and IEDF (for 9.32 sccm Air, middle row, and 27 sccm Air, bottom row). Left column are cases measured at R = 300 mm (400 mm on the right column).

kind of propulsive efficiency. Taking the data measured at $R = 400$ mm, we obtain $\eta_{conv} = 3.6-4.3$ % for 9.32 and 27 sccm Air respectively. This is higher than that estimated for Krypton, 2.7 %. Still, the uncertainties using this indirect method are large since it relies on many hypotheses that have been discussed throughout this manuscript.

V. Conclusions

The results presented here represent the first test of our institution on air-breathing electric propulsion, taking as thruster a former breadboard model of an HPT. Results have been partially compared to previous

tests performed with Krypton. The methodology to estimate thruster performances based on a set of electrostatic probes has been described in deep detail, underlining the main uncertainties on the model itself and the hypotheses that have been taken to keep it as simple but as rich as possible with the experimental data available.

Concerning the plasma results and thruster performances, though the efficiency is below 4 %, there is space for improvement since this breadboard model is not optimized for ABEP. The parametric space that has been explored is very narrow, still, there is a margin for tuning the magnetic field strength, RF Power, and some other geometric parameters.

This campaign has been useful to test the performances of the facilities when operating with air, showing some limitations on the stability of the chamber pressure and the faster heating of the cryopanels. Concerning the operation of the breadboard, the main highlight is the possibility of operating the HPT with atmospheric air in a set of stable configurations and with no noticeable negative effect on the facility's hardware or degradation with time in the general performance of the components. For example, there are no signs of oxidation of surfaces exposed to or nearby to the plasma.

In future works with thrusters for ABEP, this study suggests the need to enlarge the set of diagnostics to reduce the uncertainties identified in the methodology presented here. Beyond the use of a thrust balance for direct estimation of thruster performances[14] , which is always convenient and simple, optical emission spectroscopy would provide a footprint of the plasma plume atomic/molecular composition. On the side of electrostatic probes, an E×B probe could provide also valuable information in this regard. Finally, future campaigns combined with numerical simulations[27] shall provide some insight into possible redesign strategies to improve the performance of EPT for ABEP.

Acknowledgments

References

[1] Nicholas Crisp, Peter Roberts, Sabrina Livadiotti, Vitor Oiko, S Edmondson, Sarah Haigh, C Huyton, Luciana Sinpetru, Katharine Smith, Stephen Worrall, Jonathan Becedas, Rosa Dominguez, D González, V Hanessian, A Mølgaard, J Nielsen, M Bisgaard, Yung-An Chan, Stefanos Fasoulas, and Ameli Schwalber. The benefits of very low earth orbit for earth observation missions. *Progress in Aerospace Sciences*, 117, 08 2020.

[2] Sterge T Demetriades. A novel system for space flight using a propulsive fluid accumulator. *J. Brit. Interplanet. Soc.*, 17, 1959.

[3] T. Andreussi, E. Ferrato, and V. Giannetti. A review of air-breathing electric propulsion: from mission studies to technology verification. *Journal of Electric Propulsion*, 1:31, 2022.

[4] T. Andreussi, E. Ferrato, A. Piragino, G. Cifali, A. Rossodivita, and M. Andrenucci. Development and experimental validation of a hall effect thruster ram-ep concept. In *Space Propulsion Conference*, number SP2018-00431, Seville, Spain, 2018. Association Aéronautique et Astronautique de France.

[5] Leonid Pekker and Michael Keidar. Analysis of airbreathing hall-effect thrusters. *Journal of propulsion and power*, 28(6):1399–1405, 2012.

[6] Vittorio Giannetti, Eugenio Ferrato, and Tommaso Andreussi. On the critical parameters for feasibility and advantage of air-breathing electric propulsion systems. *Acta Astronautica*, 220:345–355, 2024.

[7] F. Romano, B. Massuti-Ballester, T. Binder, G. Herdrich, S. Fasoulas, and T. Schönherr. System analysis and test-bed for an atmosphere-breathing electric propulsion system using an inductive plasma thruster. *Acta Astronautica*, 147:114–126, 2018.

[8] F. Romano, Y.-A. Chan, G. Herdrich, C. Traub, and et al. Rf helicon-based inductive plasma thruster (ipt) design for an atmosphere-breathing electric propulsion system (abep). *Acta Astronautica*, 176:476–483, 2020.

[9] G. Herdrich and et al. System design study of a vleo satellite platform using the irs rf helicon-based plasma thruster. *Acta Astronautica*, 215:245–259, 2024.

[10] Eduardo Ahedo and Mario Merino. Two-dimensional supersonic plasma acceleration in a magnetic nozzle. *Physics of Plasmas*, 17(7):073501, 2010.

[11] Lake A Singh and Mitchell LR Walker. A review of research in low earth orbit propellant collection. *Progress in Aerospace Sciences*, 75:15–25, 2015.

[12] Adam Shabshelowitz. *Study of RF Plasma Technology Applied to Air-Breathing Electric Propulsion.* PhD thesis, 2013.

[13] J Navarro-Cavallé, M Wijnen, P Fajardo, and E Ahedo. Experimental characterization of a 1 kw helicon plasma thruster. *Vacuum*, 149:69–73, 2018.

[14] M. Wijnen, J. Navarro-Cavallé, and P. Fajardo. Mechanically amplified milli-newton thrust balance for direct thrust

measurements of electric thrusters for space propulsion. *IEEE Transactions on Instrumentation and Measurement*, 70:3505318, 2021.

[15]Alfio E Vinci, Stéphane Mazouffre, Víctor Gómez, Pablo Fajardo, and Jaume Navarro-Cavallé. Laser-induced fluorescence spectroscopy on xenon atoms and ions in the magnetic nozzle of a helicon plasma thruster. *Plasma Sources Science and Technology*, 31(9):095007, 2022.

[16]M. R. Inchingolo, M. Merino, and J. Navarro-Cavallé. Plume characterization of a waveguide ecr thruster. *Journal of Applied Physics*, 133(11):113304, 2023.

[17]Daniel L Brown, Mitchell LR Walker, James Szabo, Wensheng Huang, and John E Foster. Recommended practice for use of faraday probes in electric propulsion testing. *Journal of Propulsion and Power*, 33(3):582–613, 2016.

[18]Filippo Cichocki, Jaume Navarro-Cavallé, Alberto Modesti, and Gonzalo Ramírez Vázquez. Magnetic nozzle and rpa simulations vs. experiments for a helicon plasma thruster plume. *Frontiers in Physics*, 10, 2022.

[19]T. Tabata, T. Shirai, M. Sataka, and H. Kubo. Analytic cross sections for electron impact collisions with nitrogen molecules. *Atomic Data and Nuclear Data Tables*, 92:375–406, 2006.

[20]Y. Itikawa. Cross sections for electron collisions with nitrogen molecules. *Journal of Physical and Chemical Reference Data*, 35:31–53, 2006.

[21]Iaa database. `https://nl.lxcat.net`. Accessed: 2024-05-31.

[22]TL COTTRELL. *THE STRENGTHS OF CHEMICAL BONDS.* LONDON, BUTTERWORTHS, 1954.

[23]Y. Itikawa. Cross sections for electron collisions with oxygen molecules. *Journal of Physical and Chemical Reference Data*, 38:1–20, 2009.

[24]Francis F Chen. Langmuir probes in rf plasma: surprising validity of oml theory. *Plasma Sources Science and Technology*, 18(3):035012, 2009.

[25]Robert B. Lobbia and Brian E. Beal. Recommended practice for use of langmuir probes in electric propulsion testing. *Journal of Propulsion and Power*, 33(3):566–581, 2017.

[26]S. T. Lai and C. Miller. Retarding potential analyzer: Principles, designs, and space applications. *AIP Advances*, 10(9):095324, 2020.

[27]Pedro Jiménez, Jiewei Zhou, Jaume Navarro-Cavallé, Pablo Fajardo, Mario Merino, and Eduardo Ahedo. Analysis of a cusped helicon plasma thruster discharge. *Plasma Sources Science and Technology*, 32(10):105013, 2023.

[28]M. Martínez-Sánchez, J. Navarro-Cavallé, and E. Ahedo. Electron cooling and finite potential drop in a magnetized plasma expansion. *Physics of Plasmas*, 22(5):053501, 2015.